Pushing Rendering Boundaries: Hard Gaussian Splatting

Qingshan Xu[1]   Jiequan Cui[1]   Xuanyu Yi[1]   Yuxuan Wang[1]   Yuan Zhou[1]
Yew-Soon Ong[1,2]   Hanwang Zhang[1]

[1] Nanyang Technological University   [2] A*STAR, Singapore

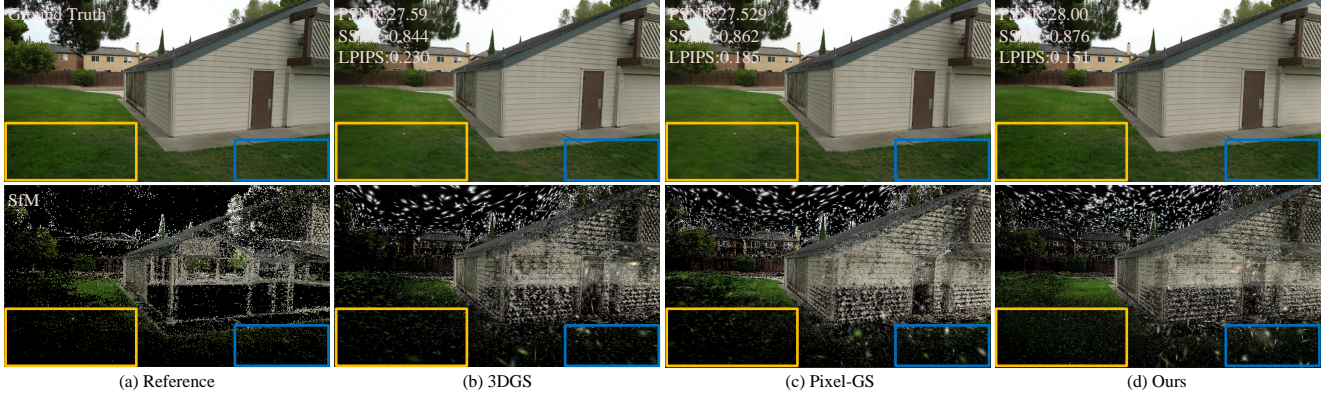(a) Reference   (b) 3DGS   (c) Pixel-GS   (d) Ours

Figure 1. **Illustration of the relationship between rendering and Gaussians distribution.** We show that 3DGS [14] and Pixel-GS [53] are unable to grow Gaussians in some challenging areas, leading to artifacts in these areas. In contrast, our method effectively grows *hard* Gaussians in these challenging areas to recover 3D scenes, thus achieving better novel view synthesis results.

Abstract

3D Gaussian Splatting (3DGS) has demonstrated impressive Novel View Synthesis (NVS) results in a real-time rendering manner. During training, it relies heavily on the average magnitude of view-space positional gradients to grow Gaussians to reduce rendering loss. However, this average operation smooths the positional gradients from different viewpoints and rendering errors from different pixels, hindering the growth and optimization of many defective Gaussians. This leads to strong spurious artifacts in some areas. To address this problem, we propose Hard Gaussian Splatting, dubbed HGS, which considers multiview significant positional gradients and rendering errors to grow hard Gaussians that fill the gaps of classical Gaussian Splatting on 3D scenes, thus achieving superior NVS results. In detail, we present positional gradient driven HGS, which leverages multi-view significant positional gradients to uncover hard Gaussians. Moreover, we propose rendering error guided HGS, which identifies noticeable pixel rendering errors and potentially over-large Gaussians to jointly mine hard Gaussians. By growing and optimizing these hard Gaussians, our method helps to resolve blurring and needle-like artifacts. Experiments on various datasets demonstrate that our method achieves state-of-the-art rendering quality while maintaining real-time efficiency. Our code will be available at `https://github.com/GhiXu/HGS`.

1. Introduction

Novel View Synthesis (NVS) is a fundamental task in computer vision and graphics, with its wide applications in virtual reality, robotics and media generation. In the past few years, Neural Radiance Field (NeRF) [24] has made significant advances in NVS. It adopts neural implicit representations to model 3D scenes via volume rendering [23]. Generally, NeRF works [1, 2, 25] require ray marching for volume rendering, which compromises on efficiency. Recently, 3D Gaussian Splatting (3DGS) [14] combines an point-based explicit representation, 3D Gaussian, with GPU-friendly differentiable rasterization for volume rendering, achieving impressive NVS results in a real-time manner.

3DGS initializes a set of 3D Gassuains from *sparse* point clouds produced by Structure from Motion (SfM) [30] to represent a scene, and gradually populates empty areas by growing existing Gaussians (the bottom row of Figures 1(a) and (b)). To select good candidates for growing, 3DGS checks if the *average* magnitude of view-space positional
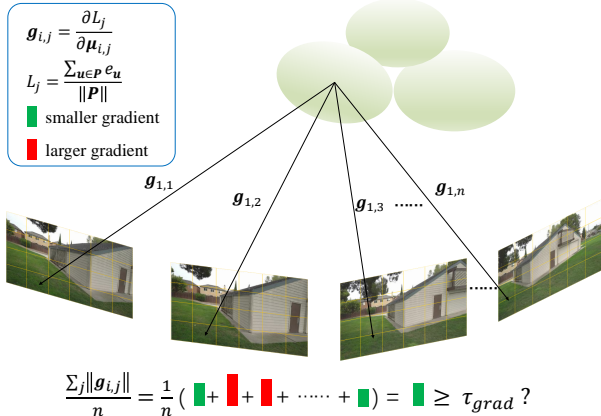
$$g_{i,j} = \frac{\partial L_j}{\partial \boldsymbol{\mu}_{i,j}}$$

$$L_j = \frac{\sum_{\boldsymbol{u} \in P} e_{\boldsymbol{u}}}{\|\boldsymbol{P}\|}$$

■ smaller gradient

■ larger gradient

$\boldsymbol{g}_{1,1}$ $\boldsymbol{g}_{1,2}$ $\boldsymbol{g}_{1,3}$ ...... $\boldsymbol{g}_{1,n}$

......

$$\frac{\sum_j \|\boldsymbol{g}_{i,j}\|}{n} = \frac{1}{n}\,(\; \blacksquare + \blacksquare + \blacksquare + \cdots\cdots + \blacksquare \;) = \blacksquare \;\geq\; \tau_{grad} \;?$$

Figure 2. **Illustration of the Gaussian growing criterion in 3DGS [14].** $\boldsymbol{g}_{i,j}$ denotes the positional gradient of Gaussian $\mathcal{G}_i$ under viewpoint j. L_j denotes the rendering loss under viewpoint j, which is computed by averaging the rendering errors $\{e_{\boldsymbol{u}}\}$ of all pixels $\boldsymbol{P}$. Larger gradients and rendering errors will be smoothed by the average operation.

gradients of each Gaussian in a growth interval is larger than a threshold, as illustrated in Figure 2. This criterion encourages Gaussians to gradually *densify* and reconstruct the entire 3D scene.

However, strong spurious artifacts remain in some challenging regions, such as areas with repetitive textures and few observations, as shown in the yellow and blue boxes in the top row of Figures 1(b) and (c). By observing the corresponding Gaussians distribution in the bottom row of Figures 1(b) and (c), we find that there are very few Gaussians in these challenging areas. This demonstrates that the growing criterion, in fact, cannot *adequately* select suitable candidates from existing Gaussians for growing, thus limiting the NVS performance of 3DGS. We define these candidates as *hard Gaussians*. Intuitively, the average operation used in the growing criterion makes it unable to reflect the larger positional gradients of some viewpoints, as shown in Figure 2. This leads to rendering inconsistency across views. Moreover, the rendering loss used to optimize 3DGS indicates the rendering quality of the entire image but fails to indicate the quality in local image regions. Therefore, the average magnitude of positional gradients cannot reflect noticeable rendering errors of certain local image regions, especially when these regions are only observed by few viewpoints. These deficiencies prevent 3DGS from growing *hard* Gaussians to achieve better NVS results.

To address these issues, we propose Hard Gaussian Splatting, dubbed HGS, to fill the gaps of classical Gaussian Splatting on 3D scenes. Our key insight is to uncover hard Gaussians from multi-view significant positional gradients and rendering errors, and grow these Gaussians for subsequent optimization. Specifically, besides the original

Gaussian growing criterion, we first present positional gradient driven HGS (Sec. 5.1). This strategy captures k largest positional gradients for each Gaussian in the growth interval. If the minimum of these positional gradients exceeds a threshold, its corresponding Gaussian is deemed as a hard Gaussian and will grow. This strategy exploits cross-view significant positional gradients to uncover hard Gaussians, thus alleviating the rendering inconsistency across views.

In addition, we propose rendering error guided HGS (Sec. 5.2). This strategy first identifies potentially overlarge Gaussians that may cause blurring artifacts in the current training image. These Gaussians are then projected into the image to calculate pixel rendering errors. If noticeable pixel rendering errors are detected from multiple viewpoints within the growth interval, the corresponding Gaussian is considered as a hard Gaussian and will grow. This strategy robustly identifies noticeable pixel rendering errors across views to mine hard Gaussians, thus reducing rendering errors in less observed regions.

Through our proposed strategies to grow and optimize hard Gaussians, our method helps to resolve blurring and needle-like artifacts, as shown in Figure 1(d). Extensive experiments on challenging benchmark datasets [2, 12, 16] demonstrate that our method achieves state-of-the-art rendering quality while maintaining real-time efficiency. In summary, our main contributions are as follows:

- We analyze the deficiencies of Gaussian growing criterion–it smooths out significant positional gradients and rendering errors of Gaussians. This hinders hard Gaussians growing, causing artifacts in challenging areas.
- We propose HGS, which mines hard Gaussians from multi-view significant positional gradients and rendering errors for growing and optimization. This alleviates cross-view rendering inconsistency and reduces rendering errors in less observed regions, significantly improving rendering performance.
- Our proposed HGS is general. In experiments, we show that it can boost both explicit Gaussian methods [14, 49, 53] and neural Gaussian methods [7, 22] to achieve better NVS results.

2. Related Work

Novel View Synthesis. NVS aims to synthesize photo-realistic images from viewpoints different from the original input viewpoints. Early image-based rendering methods [5, 12, 17, 28] leverage 3D proxy geometry to generate novel views from source images. Over the past few years, NeRF [24] has achieved impressive NVS results [1, 2, 9, 27, 34, 48] and advanced other 3D tasks [10, 26, 32, 35, 42, 44, 47]. NeRF utilizes a multi-layer perceptron (MLP) to model scenes and leverages ray marching to render images. Nevertheless, the expensive MLP evaluation

caused by ray marching hinders the real-time performance. While subsequent methods adopt more efficient representations [3, 6, 25, 31, 41] to accelerate the rendering process, they still struggle with real-time requirements.

Gaussian Splatting. 3DGS [14] employs anisotropic Gaussians [55] to represent 3D scenes and realizes rendering by differentiable rasterization. It stands out for its real-time high-quality rendering results. Therefore, it has been rapidly extended to other 3D tasks, including surface reconstruction [13, 50], physical simulation [37, 52] and 3D generation [33, 46]. To improve 3DGS, some works tackle aliasing issues by introducing 3D smoothing and 2D Mip filters [49], multi-scale Gaussians [43] and analytic integration [20]. Scaffold-GS [22] builds anchor points to guide the distribution of local 3D Gaussians. Some methods [15, 21] leverage Level-of-Detail for large-scale scene reconstruction. Although these methods enhance 3DGS, they cannot handle strong artifacts in challenging areas.

Blurring Artifacts. Since the 3D Gaussians initialized from sparse point clouds of SfM are too sparse to describe complete 3D scenes, 3DGS develops a growing strategy to densify them and improve rendering quality. However, there are still large empty areas cannot be populated due to the gradient collision [45], resulting in blurring artifacts. To address this, some approaches [45, 50] accumulate the norms of individual pixel gradients or homodirectional positional gradients to better indicate regions with significant reconstruction errors. Pixel-GS [53] considers the number of pixels covered by the Gaussian. By using these counts as weights to dynamically average the gradients from different viewpoints, it prompts the growth of large Gaussians. Mini-Splatting [8] finds that the blurry artifacts are more directly related to the rendered index of Gaussians with the maximum contribution to each pixel. It then splits Gaussians with many rendered indices to reduce these artifacts. Spacetime-GS [19] improves rendering quality at distant sparsely covered areas by sampling new Gaussians with the guidance of training error and coarse depth. In addition, some methods [18, 54] resort to geometry priors to reduce artifacts. In contrast, our method mines hard Gaussians from multi-view significant positional gradients and rendering errors, and grow these Gaussians to resolve artifacts.

3. Preliminaries

3D Gaussian Splatting. 3DGS [14] represents a 3D scene with a set of anisotropic 3D Gaussians $\{\mathcal{G}_i | i = 1, \cdots, N\}$ and renders an image using α-blending with differentiable rasterization. Each Gaussian $\mathcal{G}_i$ is parameterized by a mean vector $\boldsymbol{\mu}_i \in \mathbb{R}^{3 \times 1}$, covariance matrix $\boldsymbol{\Sigma}_i \in \mathbb{R}^{3 \times 3}$, color $\mathbf{c}_i \in \mathbb{R}^{3 \times 1}$ and opacity $\alpha_i \in \mathbb{R}$ as:

$$\mathcal{G}_i(\mathbf{x}) = \exp(-\frac{1}{2}(\mathbf{x} - \boldsymbol{\mu}_i)^T \boldsymbol{\Sigma}_i^{-1}(\mathbf{x} - \boldsymbol{\mu}_i)), \quad (1)$$

where $\mathbf{x}$ is a spatial point within the 3D scene. To render an image from viewpoint j, the 3D Gaussian $\mathcal{G}_i$ is first splatted to the 2D image plane as a 2D Gaussian $\mathcal{G}_i^{2D}$, and then α-blending is employed to compute the color of pixel $\boldsymbol{u}$ as:

$$\mathbf{c}(\boldsymbol{u}) = \sum_{i=1}^{N} w_i \mathbf{c}_i, \ w_i = \alpha_i \mathcal{G}_i^{2D}(\boldsymbol{u}) \prod_{k=1}^{i-1} (1 - \alpha_k \mathcal{G}_k^{2D}(\boldsymbol{u})). \quad (2)$$

Through the differentiable rasterization, all the attributes in 3D Gaussians are optimized by the rendering loss. 3DGS designs an adaptive density control mechanism for Gaussian growing, adding new Gaussians where significant Gaussians are found.

Scaffold-GS. As a neural Gaussian method, Scaffold-GS [22] introduces anchor points to distribute local 3D Gaussians. Each anchor is associated with a location $\mathbf{x} \in \mathbb{R}^3$ and anchor attributes $\mathcal{A} = \{\boldsymbol{f} \in \mathbb{R}^{32}, \boldsymbol{l} \in \mathbb{R}^3, \boldsymbol{o} \in \mathbb{R}^{K \times 3}\}$, where each component represents anchor context feature, scaling factor and offsets, respectively. The positions of K neural Gaussians are calculated as:

$$\{\boldsymbol{\mu}_1, \cdots, \boldsymbol{\mu}_K\} = \boldsymbol{x} + \boldsymbol{o} \cdot \boldsymbol{l}. \quad (3)$$

The properties of neural Gaussians are decoded from the anchor attributes, and then used for α-blending to render images. During the Gaussian growing stage, Scaffold-GS constructs voxel grids to find significant neural Gaussians and grow their corresponding anchor points.

4. Deficiencies in Gaussian Growing

Both explicit Gaussian methods and neural Gaussian methods leverage sparse point clouds from SfM to initialize Gaussians or anchor points, which cannot completely model a 3D scene. To make explicit/neural Gaussians better represent the scene, Gaussian growing is applied to densify existing Gaussians gradually. Since the two kinds of methods both leverage significant Gaussians for Gaussian growing, we detail how to find significant Gaussians below.

Specifically, one Gaussian will be deemed as significant when its average view-space positional gradient over M training iterations (one growth interval) satisfies:

$$\frac{\sum_j ||\boldsymbol{g}_{i,j}||}{n} \geq \tau_{\text{grad}}, \quad (4)$$

where $\boldsymbol{g}_{i,j}$ denotes the view-space positional gradient of Gaussian $\mathcal{G}_i$ under viewpoint j, n is the total number of viewpoints that Gaussian $\mathcal{G}_i$ participates in the calculation during the M iterations, and τ_{grad} is the gradient threshold. Due to the smoothing effect of the average operation in Eq. (4), some individual larger view-space positional gradients cannot drive Gaussians to grow, as shown in Figure 2. This makes Gaussian growing focus on most easy-to-learn

(a) Ground Truth   (b) Rendered image (3DGS)   (c) Rendered index   (d) Potentially over-large Gaussians   (e) Hard Gaussians
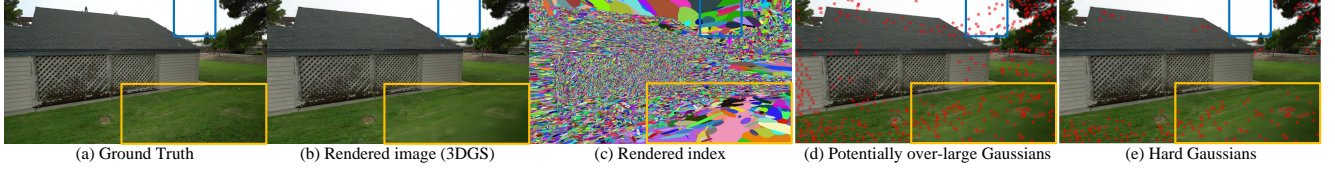
Figure 3. **Visual analysis of rendering error guided HGS.** (a) Ground truth image. (b) Rendered image by 3DGS. (c) Rendered index of Gaussians with the maximum contribution to each pixel. (d) Projection points of potentially over-large Gaussians. (e) Projection points of hard Gaussians. Potentially over-large Gaussians may indicate false positives for Gaussian growing while hard Gaussians alleviate this (the blue boxes in (d) and (e)).

viewpoints and ignore some hard-to-learn viewpoints, leading to cross-view rendering inconsistency.

Moreover, the view-space positional gradient is computed by:

$$\boldsymbol{g}_{i,j} = \frac{\partial L_j}{\partial \boldsymbol{\mu}_{i,j}}, \quad L_j = \frac{\sum_{\boldsymbol{u} \in \boldsymbol{P}} e_{\boldsymbol{u}}}{||\boldsymbol{P}||}, \quad (5)$$

where L_i denotes the rendering loss under viewpoint j, $\boldsymbol{\mu}_{i,j}$ is the pixel-space projection point of Gaussian $\mathcal{G}_i$ under viewpoint j, $\boldsymbol{P}$ is the total pixel coordinates, and $e_{\boldsymbol{u}}$ is the rendering error of pixel $\boldsymbol{u}$. Since L_j indicates the rendering quality of the entire image instead of local image regions, the resulting average view-space positional gradient fails to reflect lager local rendering errors. This prevents Gaussians from growing in regions with larger local rendering errors.

One straightforward way to alleviate the above problems is to lower the gradient threshold τ_{grad} to encourage more Gaussians to grow. However, as pointed out in [45, 53], lowering τ_{grad} will prioritize densifying the well-reconstructed areas. This will introduce *redundant Gaussians* in these areas and cannot effectively reduce artifacts (See supplementary for more analysis).

5. Hard Gaussians Splatting–HGS

To address the problems analyzed above, we propose Hard Gaussian Splatting, dubbed HGS, to uncover hard Gaussians from multi-view significant positional gradients and rendering errors. In this way, our method can grow and optimize these hard Gaussians to recover more complete 3D scenes, thereby improving rendering quality.

5.1. Positional Gradient Driven HGS

The view-space positional gradient reflects the overall image reconstruction quality under a certain viewpoint. The original Gaussian growing criterion averages the n view-space positional gradients over M iterations to find growing candidates. Although the average operation can reduce the impact of noise, it smooths some individual larger positional gradients.

In fact, the larger view-space positional gradients also indicate that their corresponding Gaussians need to populate empty areas. However, they are ignored by the original

growing criterion. Therefore, we present Positional Gradient driven HGS (PGHGS), which uncovers hard Gaussians from multi-view significant positional gradients. To reliably capture significant positional gradients, we first sort the n positional gradients for Gaussian $\mathcal{G}_i$ as:

$$\{\boldsymbol{g}'_{i,1}, \cdots, \boldsymbol{g}'_{i,n}\} = \text{sort}_{\downarrow}(\boldsymbol{g}_{i,1}, \cdots, \boldsymbol{g}_{i,n}), \quad (6)$$

where $\text{sort}_{\downarrow}$ denotes descending sort. Then, we mine hard Gaussians if the *k-th* largest positional gradient satisfies:

$$||\boldsymbol{g}'_{i,k}|| \geq \lambda \tau_{\text{grad}}, \quad (7)$$

where λ is a constant that controls the extent of excavation. By growing these hard Gaussians, the larger reconstruction errors under some individual viewpoints can be reduced. This facilitates the rendering consistency across views.

5.2. Rendering Error Guided HGS

By delving into the calculation of view-space positional gradient (Eq. (5)), we know that it is the gradient of the average rendering error with respect to the view-space projection point. Therefore, the view-space positional gradient cannot effectively reflect the reconstruction errors of some local image regions, especially when these regions are only observed by few viewpoints. To resolve this, we introduce Rendering Error guided HGS (REHGS) to link hard Gaussians with local rendering errors. However, as pixel rendering errors entangle contributions from multiple Gaussians (Eq. (2)), it is challenging to establish this link.

To this end, we leverage the Gaussians with the maximum contribution to correlate pixel rendering errors. Specifically, for pixel $\boldsymbol{u}$, its rendered index is defined as $\text{idx}(\boldsymbol{u}) = \arg\max_i w_i$. This considers the maximum Gaussian contribution in α-blending, thus reflecting the relationship between pixel rendering errors and Gaussians to some extent. On this basis, Gaussian $\mathcal{G}_i$ has the maximum rendering contribution on these pixels $\boldsymbol{S}_i = \{\boldsymbol{u}|\text{idx}(\boldsymbol{u}) = i, \boldsymbol{u} \in \boldsymbol{P}\}$. To detect noticeable local rendering errors rather than outlier pixels, we first identify potentially over-large Gaussians based on the size of $\boldsymbol{S}_i$. One Gaussian will be considered potentially over-large and prone to blurring artifacts if

it meets the following condition [8]:

$$||\boldsymbol{S}_i|| > \tau_{\text{large}}||\boldsymbol{P}||, \quad (8)$$

where τ_{large} is a threshold to control the extent of potentially large areas. This condition can efficiently find Gaussians which may lead to burring artifacts ("over-reconstruction"), as shown in the yellow boxes of Figures 3(c) and (d).

In fact, it is possible to describe low-textured areas and repetitive textures with potentially over-large Gaussians, as shown in the blue box of Figure 3(d). Therefore, using only Eq. (8) to determine the over-large Gaussians will result in false positives. To locate the Gaussians that cause blurring artifacts more accurately, we leverage rendering errors to mine hard Gaussians. For one potentially over-large Gaussian $\mathcal{G}_i$, we project it into the current training viewpoint j to obtain the corresponding pixel $\boldsymbol{u}_{i,j}$. Then, this Gaussian will be considered as a hard Gaussian if it satisfies:

$$\text{SSIM}(\boldsymbol{I}_j, \hat{\boldsymbol{I}}_j)(\boldsymbol{u}_{i,j}) < \tau_{\text{SSIM}}, \quad (9)$$

where $\boldsymbol{I}_j$ and $\hat{\boldsymbol{I}}_j$ denote the ground truth and rendered images under viewpoint j, respectively. SSIM means Structural Similarity Index Measure [36], which measures the similarity between two images. τ_{SSIM} is a threshold to judge rendering quality. Note that, SSIM is chosen because it can perform local analyssis on an image, making it suitable for detecting structure changes in the image.

With the guidance of potentially over-large Gaussians and pixel rendering errors, our method can locate hard Gaussians in truly blurring areas, as shown in Figure 3(e). Furthermore, such Gaussians should be seen by at least two views during the M iterations. This avoids unstable growth caused by hard Gaussians determined by only a single view.

5.3. Efficient HGS

In practice, as more hard Gaussians are grown and optimized, the efficiency of Gaussian splatting will be sacrificed. To better balance rendering quality and efficiency, we introduce an efficient HGS method, called Effi-HGS. Concretely, we first count the percentage of growing Gaussians selected by the original growing criterion (Eq. (4)) in each growth interval, denoted as Q. Then, during the PGHGS, we choose the top Q Gaussians as hard ones for growing based on $\{\boldsymbol{g}'_{i,k}|i = 1, \cdots, N\}$. In this way, Effi-HGS can adaptively control the number of hard Gaussians for efficiency while improving rendering quality.

6. Experiments

6.1. Experimental Setup

Datasets and Metrics. We comprehensively evaluate our methods across 17 scenes from publicly available datasets, including nine scenes from Mip-NeRF360 [2], six scenes from Tanks&Temples [16] and two scenes from Deep Blending [12]. The first two datasets contain both bounded indoor scenes and unbounded outdoor scenes. The last one is with two bounded indoor scenes. We evaluate the quality of synthesized novel views through several quantitative metrics, including Peak Signal-to-Noise Ratio (PSNR), Structural Similarity Index Measure (SSIM) [36] and Learned Perceptual Image Patch Similarity (LPIPS) [51].

Baselines and Implementations. We compare our methods against state-of-the-art NeRF and Gaussian splatting methods. The NeRF methods include Plenoxels [9], INGP [25] and Mip-NeRF360 [2], and their evaluation results are from [14]. For the Gaussian splatting methods, explicit methods, including 3DGS [14], Mip-Splatting[1] [49] and Pixel-GS [53], and the neural method, Scaffold-GS [22], are compared. We retrain these Gaussian splatting methods for 30K iterations on the same platform. We build our methods upon the Scaffold-GS repository [22]. We maintain the same threshold τ_{grad} and growing interval M for Gaussian growing as in the Scaffold-GS. We set $\{k, \lambda, \tau_{\text{large}}, \tau_{\text{SSIM}}\} = \{3, 1.0, 2\text{e-4}, 0.7\}$ across all scenes. All experiments are conducted on one NVIDIA RTX 3090 GPU with 24GB memory.

6.2. Performance Evaluation

Rendering Quality. The quantitative results on three datasets [2, 12, 16] are presented in Table 1. It can be noticed that our proposed method, HGS, achieves almost the best rendering results in all metrics on these three datasets, expect for the second best SSIM on Mip-NeRF360. Notably, HGS outperforms the state-of-the-arts by a large margin on Tanks&Temples, which contains large-scale complex scenes. Moreover, our efficient version, Effi-HGS, achieves comparable rendering results with the state-of-the-arts on Mip-NeRF360, and surpasses them on Tanks&Temples and Deep Blending.

The qualitative results are shown in Figure 4. We observe that both our proposed methods significantly reduce blurring and needle-like artifacts. In particular, it is challenging for the previous methods to reconstruct some occluded areas, such as the the top row in Figure 4. In contrast, our methods can recover these challenging areas. This can be attributed to that our approaches can mine hard Gaussians from significant positional gradients and rendering errors, and grow these Gaussians to optimize fine-scale and less observed areas.

Efficiency Comparisons. We further compare efficiency with Gaussian splatting methods in terms of training time, rendering speed and storage size. The results are reported in Table 2. As can be seen, for explicit Gaussian methods,

---

[1]The Mip-Splatting we compared is the version that has been combined with the densification in GOF [50].

Dataset	Mip-NeRF360			Tanks&Temples			Deep Blending		
Method │ Metric	PSNR ↑	SSIM ↑	LPIPS ↓	PSNR ↑	SSIM ↑	LPIPS ↓	PSNR ↑	SSIM ↑	LPIPS ↓
Plenoxels [9]	23.08	0.626	0.463	-	-	-	23.06	0.795	0.510
INGP [25]	25.59	0.699	0.331	-	-	-	23.62	0.797	0.423
Mip-NeRF360 [2]	27.69	0.792	0.237	-	-	-	29.40	0.901	0.245
3DGS [14]	27.71	0.825	0.202	24.90	0.850	0.178	29.46	0.899	0.247
Pixel-GS [53]	27.87	0.835	0.176	25.18	0.860	0.157	28.88	0.892	0.251
Mip-Splatting [49]	27.92	0.838	0.175	25.02	0.857	0.166	29.25	0.903	0.240
Scaffold-GS [22]	27.98	0.825	0.208	25.74	0.861	0.170	30.23	0.907	0.245
Effi-HGS (Ours)	28.14	0.831	0.179	26.02	0.870	0.148	30.33	0.908	0.238
HGS (Ours)	28.30	0.837	0.166	26.36	0.880	0.126	30.40	0.908	0.225

Table 1. **Quantitative comparisons on three datasets [2, 12, 16].** The best, second-best, and third-best entries are marked in red, orange, and yellow, respectively.
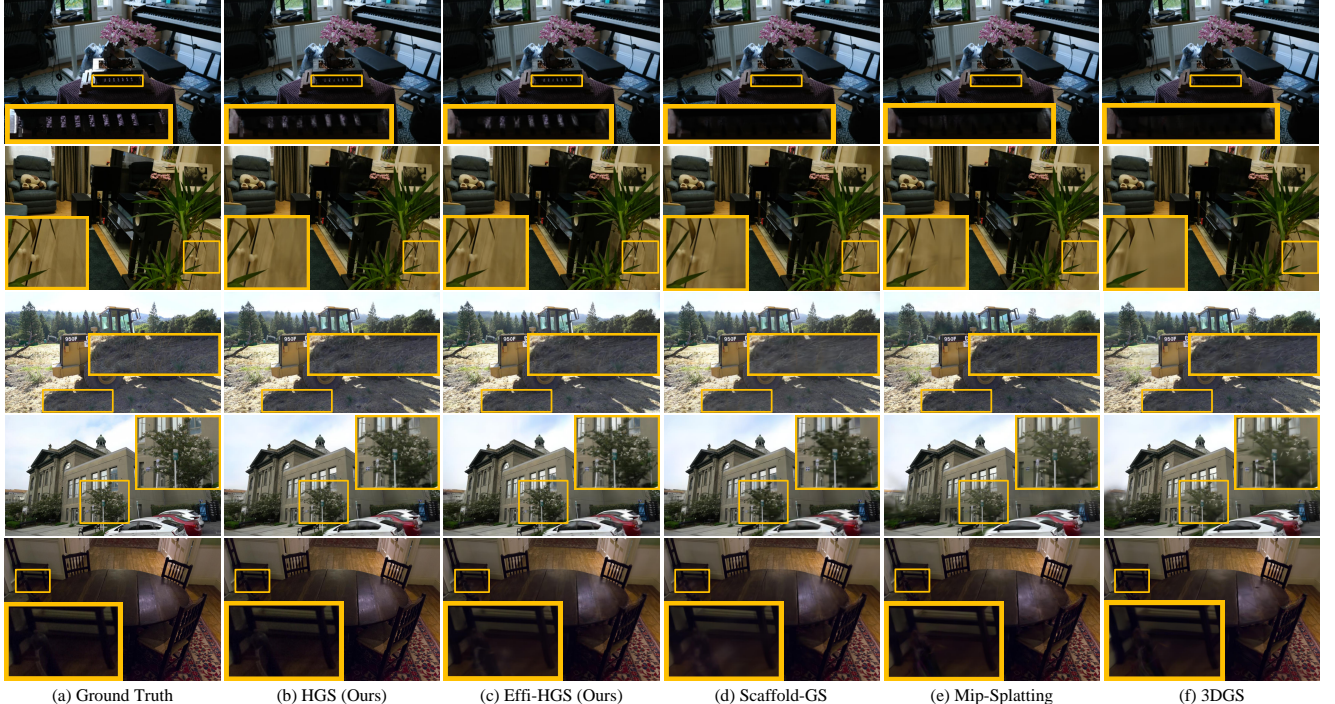

(a) Ground Truth (b) HGS (Ours) (c) Effi-HGS (Ours) (d) Scaffold-GS (e) Mip-Splatting (f) 3DGS

Figure 4. **Qualitative comparisons on three datasets [2, 12, 16].** Yellow boxes show challenging areas. Our methods can reconstruct these areas well while other methods fail.

improved rendering quality requires growing more Gaussians (larger storage size), which increases training time and reduces rendering speed. The neural Gaussian method, Scaffold-GS, can enhance both rendering quality and efficiency compared to Mip-Splatting and Pixel-GS. Similarly, since our methods will grow many hard Gaussians to improve rendering quality, this will also increase training time and reduce rendering speed. Overall, the efficiency of our methods is acceptable considering the superior rendering quality. Moreover, our efficient one achieves competitive

efficiency while showing much better rendering quality than previous methods.

6.3. Generalization Performance

To verify the generalization of our proposed approach, several state-of-the art Gaussian splatting methods are integrated with our proposed HGS to evaluate NVS on Tanks&Temples. The considered methods include 3DGS, Pixel-GS, Mip-Splatting and HAC [7]. Among them, the first three methods are explicit Gaussian methods. HAC

	PSNR ↑	SSIM ↑	LPIPS ↓	Train	FPS	Memory
3DGS [14]	24.90	0.850	0.178	**15.2m**	**159**	0.36GB
Pixel-GS [53]	25.18	0.860	0.157	26.3m	88	0.80GB
Mip-Splatting [49]	25.02	0.857	0.166	20.0m	126	0.45GB
Scaffold-GS [22]	25.74	0.861	0.170	20.4m	125	**0.18GB**
Effi-HGS (Ours)	26.02	0.870	0.148	28.6m	87	0.30GB
HGS (Ours)	**26.36**	**0.880**	**0.126**	66.2m	42	0.73GB

Table 2. **Efficiency comparisons on Tanks&Temples [16].**

Method	PSNR ↑	SSIM ↑	LPIPS ↓
3DGS [14]	24.90	0.850	0.178
Pixel-GS* [53]	25.26	0.861	0.158
Mip-Splatting* [49]	25.17	0.861	0.163
HAC [7]	25.77	0.859	0.173
3DGS + HGS	25.04	0.856	0.163
	0.14 ↑	0.006 ↑	0.015 ↓
Pixel-GS* + HGS	25.28	0.864	**0.147**
	0.02 ↑	0.003 ↑	0.011 ↓
Mip-Splatting* + HGS	25.26	0.862	0.155
	0.09 ↑	0.001 ↑	0.008 ↓
HAC + HGS	**25.96**	**0.869**	0.150
	0.19 ↑	0.010 ↑	0.023 ↓

Table 3. **Generalization performance of HGS on Tanks&Temples [16].** Pixel-GS* and Mip-Splatting* mean they are combined with opacity correction [4].

is a compact neural Gaussian method that learns structured compact hash grids for anchor attributes modeling. Considering training efficiency, we test the generalization performance of our efficient HGS. Results are reported in Table 3.

It can be seen that our proposed HGS boosts all rendering metrics for both explicit and neural Gaussian methods. Remarkably, HGS dramatically improves the LPIPS metric. Moreover, the performance improvement on neural Gaussian methods are more pronounced than on explicit Gaussian methods, as neural Gaussian methods will grow K Gaussians for each added anchor point (Eq. (3)). With our HGS, neural Gaussian methods greatly promote the Gaussian growing in poorly reconstructed regions, resulting in a more substantial performance improvement.

Note that, for Pixel-GS and Mip-Splatting that have grown more Gaussians than 3DGS with their modified gradients, in order to improve their rendering quality with our HGS, we find that it is necessary to combine them with the opacity correction [4] to remove the bias in the cloning operation first. This is because the bias will hinder the Gaussian optimization more obviously when a large number of Gaussian points are cloned simultaneously. Based on the improvement brought by the opacity correction, our HGS

	OG	PGHGS	REHGS	PSNR ↑	SSIM ↑	LPIPS ↓
Baseline	✓			25.74	0.861	0.170
Model-A	✓	✓		26.32	0.879	0.129
Model-B	✓		✓	25.99	0.867	0.155
HGS	✓	✓	✓	**26.36**	**0.880**	**0.126**

Table 4. **Ablation study on Tanks&Temples [16].** OG: Original Growing criterion. PGHGS: Positional Gradient driven HGS. RE-HGS: Rendering Error guided HGS.

can further boost the rendering performance. The results suggest that our HGS is general for both explicit and neural Gaussian methods.

6.4. Analysis

In this section, we perform ablation studies and analysis experiments on both Tanks&Temples and Deep Blending to analyze the effectiveness of our proposed designs in Sec. 5.

Ablation Study. We adopt Scaffold-GS as our baseline. Our different designs are progressively added to the baseline to investigate their efficacy. Results are reported in Table 4 (See supplementary for ablation study on Deep Blending). By adding PGHGS to the baseline, the rendering quality of Model-A has been improved a lot in all metrics (PSNR: 0.58 ↑, SSIM: 0.018 ↑, LPIPS: 0.041 ↓). As for RE-HGS, it boosts the baseline obviously and further enhances Model-A. This demonstrates that both our proposed designs can mine hard Gaussians to improve rendering quality. In addition, compared to PGHGS, REHGS tends to find noticeable rendering errors, it cannot detect some inconspicuous artifacts, which can be probed better by PGHGS. Thus, the improvement brought by PGHGS is more obvious.

Figure 5 shows how the proposed designs improve the rendering quality. Both Model-A and Model-B can reconstruct details better than Baseline, such as the distant house and front grass in the blue and yellow boxes of Figure 5. Moreover, our full model can further reduce blurring artifacts in Model-A, such as the orange boxes in Figures 5(c) and (e). These results show that our method effectively improves rendering performance.

Effect of k. k represents the number of significant positional gradients in the growth interval in Eq. (7). We vary this value to study its effect and report the results in Table 5. We observe that: 1) Reducing k can further improve LPIPS but degrade PSNR. This is because reducing k relaxes the criterion for significant positional gradients, leading to more growing Gaussians. This may introduce noise to impair PSNR. On the other hand, more Gaussians are helpful to alleviate blurring artifacts, and LPIPS is evaluated through deep image features which have anti-noise ability. Therefore, reducing k can improve LPIPS. 2) Increasing k degrades almost all rendering metrics, suggesting that PGHGS
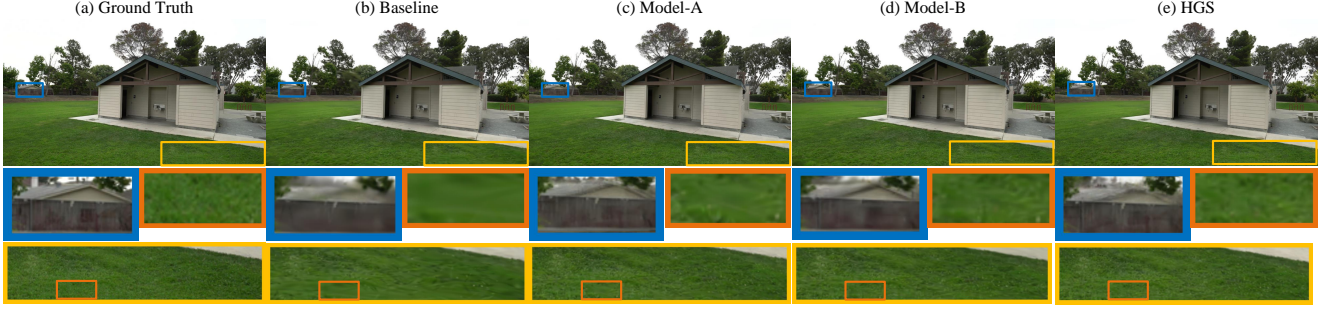
Figure 5. **Qualitative results of ablation study.**

Module	Setting	Tanks&Temples			Deep Blending		
		PSNR ↑	SSIM ↑	LPIPS ↓	PSNR ↑	SSIM ↑	LPIPS ↓
PGHGS	k=1	-	-	-	30.31	0.906	**0.211**
	k=2	26.34	**0.880**	**0.123**	30.39	**0.908**	0.219
	k=3	**26.36**	**0.880**	0.126	**30.40**	**0.908**	0.225
	k=4	26.26	0.878	0.131	30.19	**0.908**	0.230
REHGS	POG	26.26	0.879	**0.121**	30.17	0.896	**0.194**
	HG	**26.36**	**0.880**	0.126	**30.40**	**0.908**	0.225
	τ_{SSIM}=0.6	26.34	0.880	0.127	30.29	0.908	0.225
	τ_{SSIM}=0.7	26.36	0.880	**0.126**	**30.40**	0.908	0.225
	τ_{SSIM}=0.8	**26.39**	0.880	**0.126**	30.37	0.908	**0.224**
	τ_{large}=1e-4	**26.38**	**0.880**	0.125	30.35	0.908	0.225
	τ_{large}=2e-4	26.36	**0.880**	0.126	**30.40**	0.908	0.225
	τ_{large}=3e-4	26.36	0.879	0.127	30.39	0.908	0.225

Table 5. **More module analysis on both Tanks&Temples [16] and Deep Blending [12].** PGHGS: Positional Gradient driven HGS. REHGS: Rendering Error guided HGS. POG: Potentially Over-large Gaussians. HG: Hard Gaussians. - indicates no results due to out of memory error.

Figure 6. **Effect of λ.**

cannot mine hard Gaussians sufficiently when k is too large.

Effect of λ. To investigate the impact of λ in Eq (7), we set λ to different values and show the results in Figure 6. As the λ increases, the rendering quality (PSNR, SSIM and LPIPS) degrades while the training efficiency improves. This suggests that lowering λ allows for mining as many hard Gaussians as possible to improve rendering quality. Therefore, the training efficiency is reduced when a large number of Gaussians are splatted and optimized.

Potentially Over-large Gaussians or Hard Gaussians. In Sec. 5.2, we locate hard Gaussians from potentially over-large Gaussians. Here, we compare the impact of potentially over-large Gaussians (Eq. (8)) and hard Gaussians (Eq. (9)) on rendering performance in Table 4. Potentially over-large Gaussians improve LPIPS slightly but degrade PSNR a lot. As demonstrated in Sec. 5.2, potentially over-large Gaussians will overgrow the already learned areas. This makes the already learned areas susceptible to redundant Gaussians, resulting in the PSNR degradation.

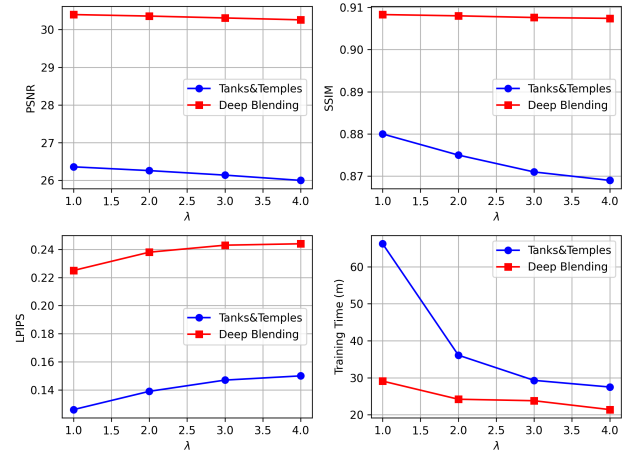**Effect of τ_{SSIM}.** We evaluate the NVS performance with different τ_{SSIM} values in Table 5. Lowering τ_{SSIM} prevents REHGS from fully identifying noticeable rendering errors, degrading NVS performance. The performance is nearly optimal with our set value, and converges at larger τ_{SSIM}.

Effect of τ_{large}. We further test the NVS performance with different τ_{large} values in Table 5. This parameter is almost insensitive to these varying values. Moreover, our selected value almost achieves the best NVS performance on both Tanks&Temples and Deep Blending.

7. Conclusion

In this work, we presented HGS, a hard Gaussians growing framework for Gaussian Splatting, which leverages multi-view significant positional gradients and rendering errors to uncover hard Gaussians. By growing and optimizing these hard Gaussians, our methods can effectively resolve blurring and needle-like artifacts in challenging areas. Our experimental results demonstrate that HGS achieves superior rendering quality while maintaining real-time rendering speed. Moreover, we verify that our HGS can boost both explicit and neural Gaussian methods, showing its potential generalization ability to other Gaussian splatting related tasks.

References

[1] Jonathan T Barron, Ben Mildenhall, Matthew Tancik, Peter Hedman, Ricardo Martin-Brualla, and Pratul P Srinivasan. Mip-nerf: A multiscale representation for anti-aliasing neural radiance fields. In *Proceedings of the IEEE International Conference on Computer Vision*, pages 5855–5864, 2021. 1, 2

[2] Jonathan T Barron, Ben Mildenhall, Dor Verbin, Pratul P Srinivasan, and Peter Hedman. Mip-nerf 360: Unbounded anti-aliased neural radiance fields. In *Proceedings of the IEEE Conference on Computer Vision and Pattern Recognition*, pages 5470–5479, 2022. 1, 2, 5, 6, 3, 4

[3] Jonathan T Barron, Ben Mildenhall, Dor Verbin, Pratul P Srinivasan, and Peter Hedman. Zip-nerf: Anti-aliased grid-based neural radiance fields. In *Proceedings of the IEEE International Conference on Computer Vision*, pages 19697–19705, 2023. 3, 4

[4] Samuel Rota Bulò, Lorenzo Porzi, and Peter Kontschieder. Revising densification in gaussian splatting. *arXiv preprint arXiv:2404.06109*, 2024. 7, 4

[5] Gaurav Chaurasia, Sylvain Duchene, Olga Sorkine-Hornung, and George Drettakis. Depth synthesis and local warps for plausible image-based navigation. *ACM transactions on graphics (TOG)*, 32(3):1–12, 2013. 2

[6] Anpei Chen, Zexiang Xu, Andreas Geiger, Jingyi Yu, and Hao Su. Tensorf: Tensorial radiance fields. In *European conference on computer vision*, pages 333–350. Springer, 2022. 3

[7] Yihang Chen, Qianyi Wu, Weiyao Lin, Mehrtash Harandi, and Jianfei Cai. Hac: Hash-grid assisted context for 3d gaussian splatting compression. In *European Conference on Computer Vision*, pages 422–438. Springer, 2025. 2, 6, 7

[8] Guangchi Fang and Bing Wang. Mini-splatting: Representing scenes with a constrained number of gaussians. *arXiv preprint arXiv:2403.14166*, 2024. 3, 5

[9] Sara Fridovich-Keil, Alex Yu, Matthew Tancik, Qinhong Chen, Benjamin Recht, and Angjoo Kanazawa. Plenoxels: Radiance fields without neural networks. In *Proceedings of the IEEE conference on computer vision and pattern recognition*, pages 5501–5510, 2022. 2, 5, 6, 3, 4

[10] Qiancheng Fu, Qingshan Xu, Yew Soon Ong, and Wenbing Tao. Geo-neus: Geometry-consistent neural implicit surfaces learning for multi-view reconstruction. *Advances in Neural Information Processing Systems*, 35:3403–3416, 2022. 2

[11] Sharath Girish, Kamal Gupta, and Abhinav Shrivastava. Eagles: Efficient accelerated 3d gaussians with lightweight encodings. *arXiv preprint arXiv:2312.04564*, 2023. 2

[12] Peter Hedman, Julien Philip, True Price, Jan-Michael Frahm, George Drettakis, and Gabriel Brostow. Deep blending for free-viewpoint image-based rendering. *ACM Transactions on Graphics (ToG)*, 37(6):1–15, 2018. 2, 5, 6, 8, 1, 4

[13] Binbin Huang, Zehao Yu, Anpei Chen, Andreas Geiger, and Shenghua Gao. 2d gaussian splatting for geometrically accurate radiance fields. In *ACM SIGGRAPH 2024 Conference Papers*, pages 1–11, 2024. 3

[14] Bernhard Kerbl, Georgios Kopanas, Thomas Leimkühler, and George Drettakis. 3d gaussian splatting for real-time radiance field rendering. *ACM Trans. Graph.*, 42(4):139–1, 2023. 1, 2, 3, 5, 6, 7, 4

[15] Bernhard Kerbl, Andreas Meuleman, Georgios Kopanas, Michael Wimmer, Alexandre Lanvin, and George Drettakis. A hierarchical 3d gaussian representation for real-time rendering of very large datasets. *ACM Transactions on Graphics (TOG)*, 43(4):1–15, 2024. 3

[16] Arno Knapitsch, Jaesik Park, Qian-Yi Zhou, and Vladlen Koltun. Tanks and temples: Benchmarking large-scale scene reconstruction. *ACM Transactions on Graphics (ToG)*, 36 (4):1–13, 2017. 2, 5, 6, 7, 8, 1, 4

[17] Georgios Kopanas, Julien Philip, Thomas Leimkühler, and George Drettakis. Point-based neural rendering with per-view optimization. In *Computer Graphics Forum*, pages 29–43. Wiley Online Library, 2021. 2

[18] Yanyan Li, Chenyu Lyu, Yan Di, Guangyao Zhai, Gim Hee Lee, and Federico Tombari. Geogaussian: Geometry-aware gaussian splatting for scene rendering. In *European Conference on Computer Vision*, pages 441–457. Springer, 2025. 3

[19] Zhan Li, Zhang Chen, Zhong Li, and Yi Xu. Spacetime gaussian feature splatting for real-time dynamic view synthesis. In *Proceedings of the IEEE Conference on Computer Vision and Pattern Recognition*, pages 8508–8520, 2024. 3

[20] Zhihao Liang, Qi Zhang, Wenbo Hu, Ying Feng, Lei Zhu, and Kui Jia. Analytic-splatting: Anti-aliased 3d gaussian splatting via analytic integration. *arXiv preprint arXiv:2403.11056*, 2024. 3

[21] Yang Liu, Chuanchen Luo, Lue Fan, Naiyan Wang, Junran Peng, and Zhaoxiang Zhang. Citygaussian: Real-time high-quality large-scale scene rendering with gaussians. In *European Conference on Computer Vision*, pages 265–282. Springer, 2025. 3

[22] Tao Lu, Mulin Yu, Linning Xu, Yuanbo Xiangli, Limin Wang, Dahua Lin, and Bo Dai. Scaffold-gs: Structured 3d gaussians for view-adaptive rendering. In *Proceedings of the IEEE Conference on Computer Vision and Pattern Recognition*, pages 20654–20664, 2024. 2, 3, 5, 6, 7, 1, 4

[23] Nelson Max. Optical models for direct volume rendering. *IEEE Transactions on Visualization and Computer Graphics*, 1(2):99–108, 1995. 1

[24] Ben Mildenhall, Pratul P Srinivasan, Matthew Tancik, Jonathan T Barron, Ravi Ramamoorthi, and Ren Ng. Nerf: Representing scenes as neural radiance fields for view synthesis. *Communications of the ACM*, 65(1):99–106, 2021. 1, 2

[25] Thomas Müller, Alex Evans, Christoph Schied, and Alexander Keller. Instant neural graphics primitives with a multiresolution hash encoding. *ACM transactions on graphics (TOG)*, 41(4):1–15, 2022. 1, 3, 5, 6, 4

[26] Ben Poole, Ajay Jain, Jonathan T Barron, and Ben Mildenhall. Dreamfusion: Text-to-3d using 2d diffusion. *arXiv preprint arXiv:2209.14988*, 2022. 2

[27] Christian Reiser, Songyou Peng, Yiyi Liao, and Andreas Geiger. Kilonerf: Speeding up neural radiance fields with thousands of tiny mlps. In *Proceedings of the IEEE international conference on computer vision*, pages 14335–14345, 2021. 2

9

[28] Gernot Riegler and Vladlen Koltun. Free view synthesis. In *Proceedings of the European Conference on Computer Vision*, pages 623–640. Springer, 2020. 2

[29] Sudipta Sinha, Drew Steedly, and Rick Szeliski. Piecewise planar stereo for image-based rendering. In *Proceedings of the IEEE International Conference on Computer Vision*, pages 1881–1888, 2009. 2

[30] Noah Snavely, Steven M Seitz, and Richard Szeliski. Photo tourism: exploring photo collections in 3d. In *ACM siggraph 2006 papers*, pages 835–846. 2006. 1

[31] Cheng Sun, Min Sun, and Hwann-Tzong Chen. Direct voxel grid optimization: Super-fast convergence for radiance fields reconstruction. In *Proceedings of the IEEE conference on computer vision and pattern recognition*, pages 5459–5469, 2022. 3

[32] Xiaotian Sun, Qingshan Xu, Xinjie Yang, Yu Zang, and Cheng Wang. Global and hierarchical geometry consistency priors for few-shot nerfs in indoor scenes. In *Proceedings of the IEEE Conference on Computer Vision and Pattern Recognition*, pages 20530–20539, 2024. 2

[33] Jiaxiang Tang, Jiawei Ren, Hang Zhou, Ziwei Liu, and Gang Zeng. Dreamgaussian: Generative gaussian splatting for efficient 3d content creation. *arXiv preprint arXiv:2309.16653*, 2023. 3

[34] Dor Verbin, Peter Hedman, Ben Mildenhall, Todd Zickler, Jonathan T Barron, and Pratul P Srinivasan. Ref-nerf: Structured view-dependent appearance for neural radiance fields. In *2022 IEEE Conference on Computer Vision and Pattern Recognition*, pages 5481–5490. IEEE, 2022. 2

[35] Peng Wang, Lingjie Liu, Yuan Liu, Christian Theobalt, Taku Komura, and Wenping Wang. Neus: Learning neural implicit surfaces by volume rendering for multi-view reconstruction. *Advances in Neural Information Processing Systems*, 2021. 2

[36] Zhou Wang, Alan C Bovik, Hamid R Sheikh, and Eero P Simoncelli. Image quality assessment: from error visibility to structural similarity. *IEEE transactions on image processing*, 13(4):600–612, 2004. 5

[37] Tianyi Xie, Zeshun Zong, Yuxing Qiu, Xuan Li, Yutao Feng, Yin Yang, and Chenfanfu Jiang. Physgaussian: Physics-integrated 3d gaussians for generative dynamics. In *Proceedings of the IEEE Conference on Computer Vision and Pattern Recognition*, pages 4389–4398, 2024. 3

[38] Qingshan Xu and Wenbing Tao. Multi-scale geometric consistency guided multi-view stereo. In *Proceedings of the IEEE conference on computer vision and pattern recognition*, pages 5483–5492, 2019. 2

[39] Qingshan Xu and Wenbing Tao. Planar prior assisted patchmatch multi-view stereo. In *Proceedings of the AAAI conference on artificial intelligence*, pages 12516–12523, 2020. 2

[40] Qingshan Xu, Weihang Kong, Wenbing Tao, and Marc Pollefeys. Multi-scale geometric consistency guided and planar prior assisted multi-view stereo. *IEEE Transactions on Pattern Analysis and Machine Intelligence*, 45(4):4945–4963, 2022. 2

[41] Qiangeng Xu, Zexiang Xu, Julien Philip, Sai Bi, Zhixin Shu, Kalyan Sunkavalli, and Ulrich Neumann. Point-nerf: Point-based neural radiance fields. In *Proceedings of the IEEE conference on computer vision and pattern recognition*, pages 5438–5448, 2022. 3

[42] Qingshan Xu, Xuanyu Yi, Jianyao Xu, Wenbing Tao, Yew-Soon Ong, and Hanwang Zhang. Few-shot nerf by adaptive rendering loss regularization. *arXiv preprint arXiv:2410.17839*, 2024. 2

[43] Zhiwen Yan, Weng Fei Low, Yu Chen, and Gim Hee Lee. Multi-scale 3d gaussian splatting for anti-aliased rendering. In *Proceedings of the IEEE Conference on Computer Vision and Pattern Recognition*, pages 20923–20931, 2024. 3, 2

[44] Lior Yariv, Jiatao Gu, Yoni Kasten, and Yaron Lipman. Volume rendering of neural implicit surfaces. *Advances in Neural Information Processing Systems*, 34:4805–4815, 2021. 2

[45] Zongxin Ye, Wenyu Li, Sidun Liu, Peng Qiao, and Yong Dou. Absgs: Recovering fine details in 3d gaussian splatting. In *ACM Multimedia 2024*, 2024. 3, 4, 1

[46] Xuanyu Yi, Zike Wu, Qiuhong Shen, Qingshan Xu, Pan Zhou, Joo-Hwee Lim, Shuicheng Yan, Xinchao Wang, and Hanwang Zhang. Mvgamba: Unify 3d content generation as state space sequence modeling. *arXiv preprint arXiv:2406.06367*, 2024. 3

[47] Xuanyu Yi, Zike Wu, Qingshan Xu, Pan Zhou, Joo-Hwee Lim, and Hanwang Zhang. Diffusion time-step curriculum for one image to 3d generation. In *Proceedings of the IEEE Conference on Computer Vision and Pattern Recognition*, pages 9948–9958, 2024. 2

[48] Alex Yu, Ruilong Li, Matthew Tancik, Hao Li, Ren Ng, and Angjoo Kanazawa. Plenoctrees for real-time rendering of neural radiance fields. In *Proceedings of the IEEE International Conference on Computer Vision*, pages 5752–5761, 2021. 2

[49] Zehao Yu, Anpei Chen, Binbin Huang, Torsten Sattler, and Andreas Geiger. Mip-splatting: Alias-free 3d gaussian splatting. In *Proceedings of the IEEE Conference on Computer Vision and Pattern Recognition*, pages 19447–19456, 2024. 2, 3, 5, 6, 7, 1, 4

[50] Zehao Yu, Torsten Sattler, and Andreas Geiger. Gaussian opacity fields: Efficient and compact surface reconstruction in unbounded scenes. *arXiv preprint arXiv:2404.10772*, 2024. 3, 5

[51] Richard Zhang, Phillip Isola, Alexei A Efros, Eli Shechtman, and Oliver Wang. The unreasonable effectiveness of deep features as a perceptual metric. In *Proceedings of the IEEE conference on computer vision and pattern recognition*, pages 586–595, 2018. 5

[52] Tianyuan Zhang, Hong-Xing Yu, Rundi Wu, Brandon Y Feng, Changxi Zheng, Noah Snavely, Jiajun Wu, and William T Freeman. Physdreamer: Physics-based interaction with 3d objects via video generation. In *European Conference on Computer Vision*, pages 388–406. Springer, 2025. 3

[53] Zheng Zhang, Wenbo Hu, Yixing Lao, Tong He, and Hengshuang Zhao. Pixel-gs: Density control with pixel-aware gradient for 3d gaussian splatting. *arXiv preprint arXiv:2403.15530*, 2024. 1, 2, 3, 4, 5, 6, 7

[54] Zehao Zhu, Zhiwen Fan, Yifan Jiang, and Zhangyang Wang. Fsgs: Real-time few-shot view synthesis using gaussian splatting. In *European Conference on Computer Vision*, pages 145–163. Springer, 2025. 3

[55] Matthias Zwicker, Hanspeter Pfister, Jeroen Van Baar, and Markus Gross. Ewa volume splatting. In *Proceedings Visualization, 2001. VIS'01.*, pages 29–538. IEEE, 2001. 3

Pushing Rendering Boundaries: Hard Gaussian Splatting

Supplementary Material

In this **supplementary document**, we first provide more analysis for the original Gaussian growing in Section 8. Then, we report implementation details, additional ablation study and experimental results in Section 9, Section 10 and Section 11, respectively. Next, we show the anti-aliasing ability of Mip-Splatting [49] when combined with our method in Section 12. Finally, we present discussions and limitations in Section 13.

8. More Analysis of Gaussian Growing

Since the strong artifacts in some areas can be attributed to insufficient Gaussians in these areas, one possible way to encourage Gaussians growing in these areas is to lower the gradient threshold τ_{grad} in Eq. (4). However, previous studies [45, 53] have pointed out that lowering the threshold for 3DGS [14] will preferentially grow the Gaussians in well-reconstructed areas. This cannot effectively alleviate the artifacts. Here, we further study the impact of lowering τ_{grad} for the neural Gaussian method, Scaffold-GS [22].

We conduct experiments on Mip-NeRF360 dataset [2] by lowering τ_{grad} from 2.0e-4 to 7.0e-5 for Scaffold-GS to make the final optimized number of Gaussian points comparable to our HGS. The quantitative and qualitative results are shown in Table 6 and Figure 7, respectively. We observe that: 1) Lowering τ_{grad} can boost rendering performance for Scaffold-GS. However, the improved performance still falls behind ours. 2) Lowering τ_{grad} still cannot reduce artifacts effectively, as shown in the yellow boxes of Figure 7. This is because lowering τ_{grad} tends to grow unnecessary Gaussians in areas where Gaussian points are already dense, while regions with poor reconstruction are largely unaffected. In contrast, our HGS aims to identify hard Gaussians in poorly reconstructed areas. By focusing on growing and optimizing these Gaussians, our HGS can improve rendering quality more effectively.

	τ_{grad}	PSNR ↑	SSIM ↑	LPIPS ↓	Memory
Scaffold-GS [22]	2.0e-4	27.98	0.825	0.208	**0.17GB**
	7.0e-5	28.27	0.835	0.174	0.64GB
HGS (Ours)	2.0e-4	**28.30**	**0.837**	**0.166**	0.57GB

Table 6. **Impact of lowering τ_{grad} on the Mip-NeRF360 dataset [16].**

9. Implementation Details

Following previous practices [14, 49, 53], indoor scenes are downsampled by a factor of 2 and outdoor scenes by 4 for the Mip-NeRF360 dataset [2]. Note that, we achieve this by adopting the downsampling implementation provided by the 3DGS repository instead of directly using the downsampled images provided by Mip-NeRF360 dataset. All scenes on the Tanks&Temples dataset [16] are downsampled by a factor of 2 while the scenes on the Deep Blending dataset [12] use full-resolution images. In addition, we also evaluate our methods using the downsamled images provided by the Mip-NeRF360 dataset, the results are reported in Table 7. Our HGS still significantly outperforms SOTA methods in terms of PSNR and LPIPS metrics. Effi-HGS achieves competitive performance with SOTA methods.

	PSNR ↑	SSIM ↑	LPIPS ↓
3DGS [14]	27.41	0.813	0.218
Pixel-GS [53]	27.53	0.822	0.191
Mip-Splatting [49]	27.65	0.828	0.188
Scaffold-GS [22]	27.67	0.812	0.223
Effi-HGS (Ours)	27.92	0.823	0.203
HGS (Ours)	28.06	0.827	0.182

Table 7. **Quantitative results on the Mip-NeRF360 dataset [2] using its provided downsampled images.**

10. Additional Ablation Study

We show additional ablation study results in Table 8. These results further support our analysis made in Section 6.4.

	OG	PGHGS	REHGS	PSNR ↑	SSIM ↑	LPIPS ↓
Baseline	✓			30.23	0.907	0.245
Model-A	✓	✓		30.33	**0.908**	**0.225**
Model-B	✓		✓	30.32	0.907	0.245
HGS	✓	✓	✓	**30.40**	**0.908**	**0.225**

Table 8. **Ablation study on Deep Blending [16].** OG: Original Growing criterion. PGHGS: Positional Gradient driven HGS. RE-HGS: Rendering Error guided HGS.

11. Additional Results

In this section, we provide more qualitative and quantitative results on Mip-NeRF360 [2], Tanks&Temples [16] and Deep Blending [12].

Tables 9, 10 and 11 show per-scene quantitative results on the Mip-NeRF360, Tanks&Temples and Deep Blending, respectively. Our HGS achieves the best performance on
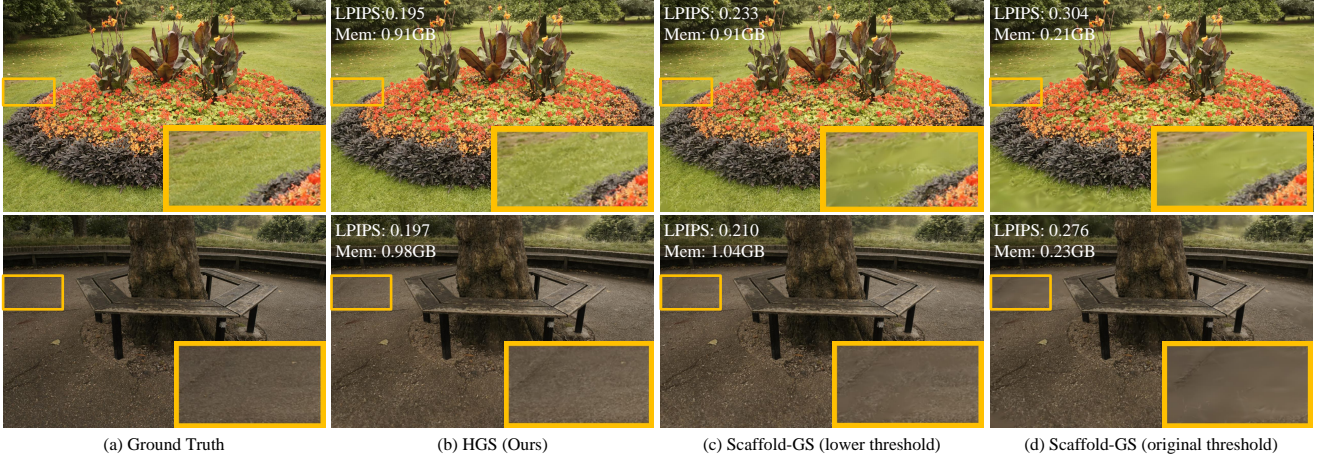
| (a) Ground Truth | (b) HGS (Ours) | (c) Scaffold-GS (lower threshold) | (d) Scaffold-GS (original threshold) |

Figure 7. **Visual analysis of lowering τ_{grad} on the Mip-NeRF360 dataset [2].**

most scenes of these datasets. Meanwhile, our Effi-HGS almost achieves the second-best performance. These detailed per-scene results further demonstrate the effectiveness of our proposed methods. Moreover, the results in Figure 8 show that our methods can reconstruct challenging details to reduce artifacts.

12. Impact for Anti-aliasing Ability

We further investigate the impact of our method for anti-aliasing ability of Mip-Splatting [49] on Mip-NeRF360 dataset [2]. Results are reported in Table 12. We observe that our method can further improve the anti-aliasing ability for Mip-Splatting, further demonstrating its potential generalization ability to other Gaussian splatting related tasks.

13. Discussions and Limitations

Like previous methods [14, 22], our methods rely on sparse point clouds from SfM to initialize Gaussian points and then grow new Gaussians from existing Gaussians gradually. This may require a longer growth process for distant regions that are not reconstructed well. One possible way to accelerate this process is to introduce structured geometry priors [29, 39, 40] to guide the growing for these areas. Additionally, since our methods grow more Gaussians to boost rendering quality, their efficiency decreases slightly. Designing an efficient coarse-to-fine/multi-scale training strategy [11, 38, 43] is an avenue for future work.

	bicycle	flowers	garden	stump	treehill	room	counter	kitchen	bonsai
				PSNR ↑					
Plenoxels [9]	21.91	20.10	23.49	20.66	22.25	27.59	23.62	23.42	24.67
INGP [25]	22.19	20.35	24.60	23.63	22.36	29.27	26.44	28.55	30.34
Mip-NeRF360 [2]	24.37	21.73	26.98	26.40	22.87	31.63	29.55	32.23	33.46
3DGS [14]	25.59	21.84	27.74	26.92	22.80	31.63	29.11	31.45	32.30
Pixel-GS [53]	25.74	21.93	27.88	27.17	22.55	31.84	29.26	31.81	32.64
Mip-Splatting [49]	25.94	22.00	27.97	27.21	22.61	31.81	29.36	31.93	32.50
Scaffold-GS [22]	25.68	21.71	27.83	26.83	23.45	32.10	29.66	31.80	32.74
Effi-HGS (Ours)	25.88	21.66	28.06	27.23	23.14	32.38	29.88	31.94	33.13
HGS (Ours)	25.94	21.94	28.33	27.28	23.06	32.61	30.26	31.63	33.64
				SSIM ↑					
	bicycle	flowers	garden	stump	treehill	room	counter	kitchen	bonsai
Plenoxels [9]	0.496	0.431	0.606	0.523	0.509	0.842	0.759	0.648	0.814
INGP [25]	0.491	0.450	0.649	0.574	0.518	0.855	0.798	0.818	0.890
Mip-NeRF360 [2]	0.685	0.583	0.813	0.744	0.632	0.913	0.894	0.920	0.941
3DGS [14]	0.777	0.621	0.874	0.784	0.653	0.927	0.914	0.932	0.947
Pixel-GS [53]	0.792	0.653	0.878	0.797	0.653	0.930	0.920	0.936	0.951
Mip-Splatting [49]	0.804	0.655	0.884	0.802	0.656	0.933	0.920	0.936	0.951
Scaffold-GS [22]	0.773	0.611	0.869	0.777	0.661	0.931	0.918	0.933	0.948
Effi-HGS (Ours)	0.787	0.631	0.877	0.793	0.644	0.934	0.922	0.934	0.952
HGS (Ours)	0.797	0.646	0.884	0.797	0.652	0.938	0.928	0.932	0.956
				LPIPS ↓					
	bicycle	flowers	garden	stump	treehill	room	counter	kitchen	bonsai
Plenoxels [9]	0.506	0.521	0.386	0.503	0.540	0.419	0.441	0.447	0.398
INGP [25]	0.487	0.481	0.312	0.450	0.489	0.301	0.342	0.254	0.227
Mip-NeRF360 [2]	0.301	0.344	0.170	0.261	0.339	0.211	0.204	0.127	0.176
3DGS [14]	0.205	0.330	0.103	0.207	0.318	0.192	0.179	0.114	0.174
Pixel-GS [53]	0.173	0.254	0.093	0.180	0.269	0.183	0.163	0.106	0.161
Mip-Splatting [49]	0.162	0.266	0.090	0.181	0.270	0.175	0.165	0.107	0.157
Scaffold-GS [22]	0.223	0.340	0.111	0.229	0.315	0.183	0.177	0.115	0.173
Effi-HGS (Ours)	0.186	0.265	0.097	0.190	0.265	0.174	0.164	0.110	0.162
HGS (Ours)	0.165	0.247	0.086	0.183	0.242	0.163	0.149	0.112	0.148

Table 9. **Per-scene quantitative results on the Mip-NeRF 360 dataset [2].**

	PSNR ↑					
	Barn	*Caterpillar*	*Courthouse*	*Ignatius*	*Meetingroom*	*Truck*
3DGS [14]	28.79	24.08	22.57	22.31	26.04	25.61
Pixel-GS [53]	29.38	24.42	22.80	22.66	26.07	25.71
Mip-Splatting [49]	29.60	24.17	21.99	22.26	26.13	25.97
Scaffold-GS [22]	29.57	24.60	23.57	23.38	27.12	26.18
Effi-HGS (Ours)	29.92	24.86	23.97	23.78	27.31	26.30
HGS (Ours)	30.49	25.53	24.26	23.78	27.63	26.46

	SSIM ↑					
	Barn	*Caterpillar*	*Courthouse*	*Ignatius*	*Meetingroom*	*Truck*
3DGS [14]	0.879	0.822	0.797	0.824	0.890	0.886
Pixel-GS [53]	0.897	0.844	0.803	0.833	0.890	0.891
Mip-Splatting [49]	0.900	0.834	0.783	0.831	0.896	0.899
Scaffold-GS [22]	0.889	0.828	0.821	0.833	0.902	0.891
Effi-HGS (Ours)	0.901	0.845	0.834	0.841	0.906	0.895
HGS (Ours)	0.914	0.867	0.841	0.845	0.911	0.900

	LPIPS ↓					
	Barn	*Caterpillar*	*Courthouse*	*Ignatius*	*Meetingroom*	*Truck*
3DGS [14]	0.170	0.198	0.245	0.159	0.160	0.137
Pixel-GS [53]	0.133	0.161	0.236	0.142	0.156	0.112
Mip-Splatting [49]	0.142	0.181	0.261	0.149	0.150	0.116
Scaffold-GS [22]	0.156	0.200	0.215	0.156	0.159	0.132
Effi-HGS (Ours)	0.128	0.170	0.191	0.136	0.146	0.114
HGS (Ours)	0.100	0.134	0.180	0.122	0.129	0.092

Table 10. **Per-scene quantitative results on the Tanks&Temples dataset [16].**

	PSNR ↑		SSIM ↑		LPIPS ↓	
	Dr Johnson	*Playroom*	*Dr Johnson*	*Playroom*	*Dr Johnson*	*Playroom*
Plenoxels [9]	23.14	22.98	0.787	0.802	0.521	0.499
INGP [25]	27.75	19.48	0.839	0.754	0.381	0.465
Mip-NeRF360 [2]	29.14	29.66	0.901	0.900	0.237	0.252
3DGS [14]	29.05	29.88	0.898	0.900	0.247	0.246
Pixel-GS [53]	28.02	29.74	0.885	0.899	0.257	0.244
Mip-Splatting [49]	28.75	29.74	0.899	0.907	0.243	0.236
Scaffold-GS [22]	29.74	30.73	0.906	0.908	0.243	0.247
Effi-HGS (Ours)	29.79	30.87	0.908	0.908	0.235	0.240
HGS (Ours)	29.92	30.89	0.908	0.908	0.225	0.225

Table 11. **Per-scene quantitative results on the Deep Blending dataset [12].**

	PSNR ↑					SSIM ↑					LPIPS ↓				
	1× Res.	2× Res.	4× Res.	8× Res.	Avg.	1× Res.	2× Res.	4× Res.	8× Res.	Avg.	1× Res.	2× Res.	4× Res.	8× Res.	Avg.
INGP [25]	26.79	24.76	24.27	24.27	25.02	0.746	0.639	0.626	0.698	0.677	0.239	0.367	0.445	0.475	0.382
Mip-NeRF360 [2]	29.26	25.18	24.16	24.10	25.67	0.860	0.727	0.670	0.706	0.741	0.122	0.260	0.370	0.428	0.295
zip-NeRF [3]	29.66	23.27	20.87	20.27	23.52	0.875	0.696	0.565	0.559	0.674	0.097	0.257	0.421	0.494	0.318
3DGS [14]	29.19	23.50	20.71	19.59	23.25	0.880	0.740	0.619	0.619	0.715	0.107	0.243	0.394	0.476	0.305
Mip-Splatting	29.39	27.48	26.54	26.29	27.43	0.890	0.815	0.759	0.768	0.808	0.092	0.188	0.292	0.385	0.239
Mip-Splatting*	29.51	27.49	26.54	26.30	27.46	0.890	0.814	0.758	0.767	0.807	0.093	0.192	0.295	0.388	0.242
Mip-Splatting* + HGS (Ours)	29.58	27.54	26.57	26.31	27.50	0.891	0.818	0.762	0.767	0.809	0.088	0.183	0.287	0.383	0.235

Table 12. **Single-scale training and multi-scale testing on the Mip-NeRF360 dataset [2].** All methods are trained on the smallest scale (1×) and evaluated across four scales (1×, 2×, 4×, and 8×), with evaluations at higher sampling rates simulating zoom-in effects. Mip-Splatting* means it is combined with opacity correction [4].

4

(a) Ground Truth   (b) HGS (Ours)   (c) Effi-HGS (Ours)   (d) Scaffold-GS   (e) Mip-Splatting   (f) 3DGS
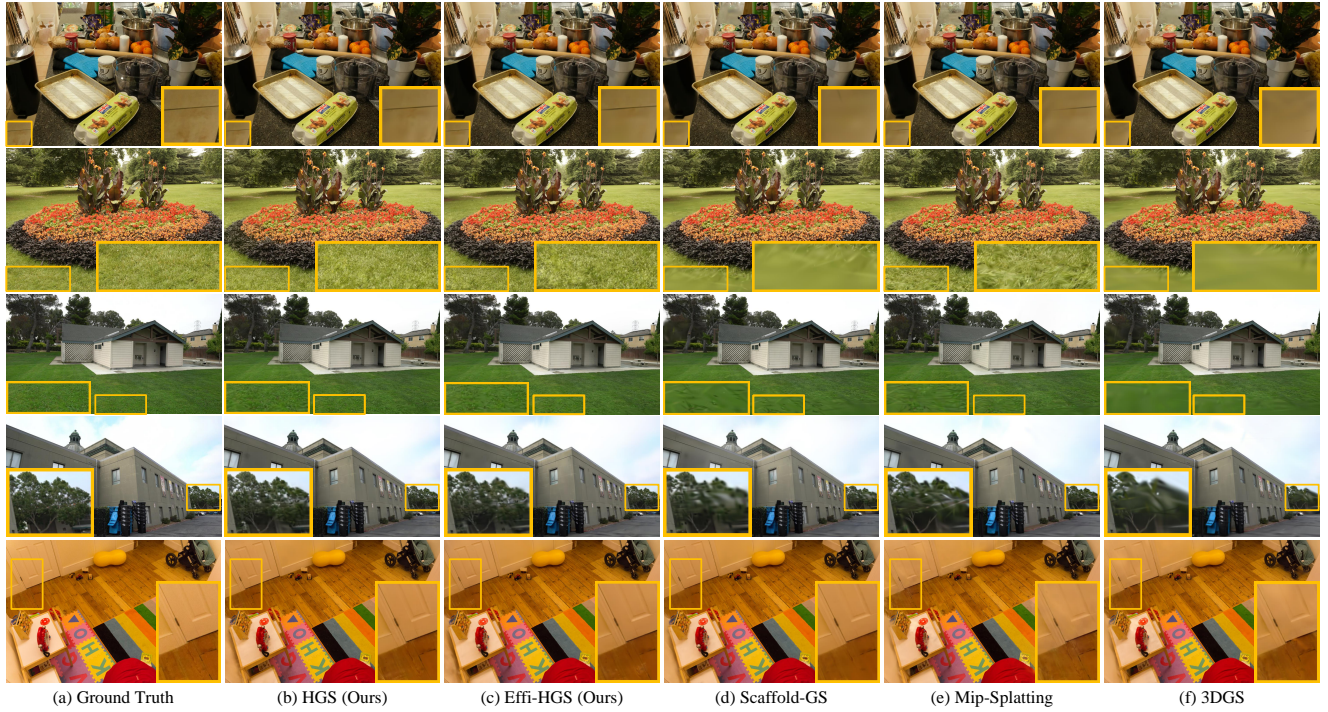
Figure 8. **More qualitative comparisons on three datasets [2, 12, 16].** Yellow boxes show challenging areas. Our methods can reconstruct these areas well while other methods fail.